KSME

Springer

Journal of Mechanical Science and Technology 37 (12) 2023

Original Article
DOI 10.1007/s12206-023-1108-z

Keywords:
· Force-transmission characteristics
· Cable-driven mechanism
· High initial velocity
· Spacecraft separation
· Ground tests

Correspondence to:
Xiaoqiang Tang
tang-xq@mail.tsinghua.edu.cn;
Qunzhi Li
13681332025@139.com

Citation:
Hou, S., Li, D., Li, Q., Tang, X. (2023). Force-transmission characteristics of a cable-driven mechanism with high initial velocity for spacecraft separation in ground tests. Journal of Mechanical Science and Technology 37 (12) (2023) 6311~6324.
http://doi.org/10.1007/s12206-023-1108-z

Received March 28th, 2023
Revised June 23rd, 2023
Accepted August 30th, 2023

† Recommended by Editor
No-cheol Park

Force-transmission characteristics of a cable-driven mechanism with high initial velocity for spacecraft separation in ground tests

Senhao Hou[1], Dongxing Li[1], Qunzhi Li[2] and Xiaoqiang Tang[1,3]

[1]Beijing Key Lab of Precision/Ultra-precision Manufacturing Equipments and Control, Tsinghua University, Beijing 100084, China, [2]Beijing Institute of Spacecraft System Engineering, Beijing 100094, China, [3]State Key Laboratory of Tribology, Department of Mechanical Engineering, Tsinghua University, Beijing 100084, China

Abstract In deep space exploration, the high-speed separation process of spacecraft is fraught with uncertainty and uncontrollability. To accurately simulate and analyze this process, a series of ground tests are typically required. In this study, a cable-driven mechanism is proposed to simulate this process. Given the high initial velocity of the spacecraft, the cable force undergoes violent fluctuations. Thus, a detailed study of the mechanism governing the force-transmission characteristics is essential to enhance the accuracy of cable force application. Three key parameters, such as slack time, peak cable force, and average relative error, are proposed to illustrate force-transmission characteristics. The effects of parameters such as thrust, pre-tension, and Young's modulus on force-transmission characteristics are also investigated. An input force planning algorithm is proposed to improve the accuracy of the cable force. High-speed separation tests are conducted within certain upper and lower bounds, and the experimental and simulation data demonstrate good agreement, confirming the accuracy of the proposed model.

1. Introduction

Deep space exploration is currently a major focus of the scientific community. Spacecraft play a critical role in this exploration, and there are numerous circumstances in which components are separated at a high speed. For example, the Mars Rover's heatshield separates from the lander at a high speed, propelled by the pyrotechnics [1]. Similarly, the process of lunar sample return or manned spacecraft return to Earth is called high speed re-entry, where the spacecraft is dramatically slowed by an ejected parachute [2]. NASA's Mars sample return (MSR) proposed a vertically ejected controlled tip-off release (VECTOR) system, which pitches the rocket up and away from the Martian surface at a high initial velocity [3]. In all of these scenarios, the separated part is instantaneously accelerated to a high initial velocity by an energy storage device, such as pyrotechnics or springs, and thereafter continues to separate under the action of inertia and external forces. Due to the presence of this energy storage device, typically, the process of high-speed separation involves two steps: short-term separation and long-term separation [4]. As shown in Fig. 1, an energy storage device, like a set of springs, releases a large amount of energy to give the separated part a high velocity, which is the short-term separation. After this, the separated part moves away under the action of external forces, which is the long-term separation.

Owning to the aerodynamic coupling effect, there is an attraction between the separated part and the unseparated part, causing the separated part to not move away quickly enough. In an extreme scenario, the separated part may have been blown backward after it was ejected, smashing into the probe and permanently disabling it. Facing such a difficult challenge, aca-

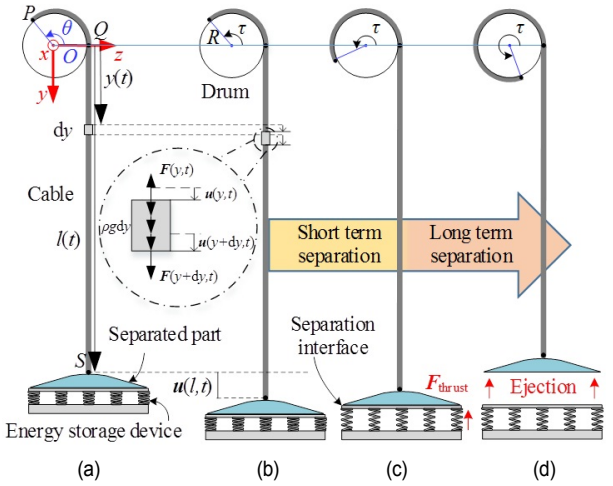

Fig. 1. Working principle of the cable-driven mechanism for high-speed separation: (a) the reference configuration; (b) details of the cable force acting on the micro element; (c) cable force in short term separation; (d) cable force in long term separation.

demics have tried many ground tests to simulate the above process. In the 1970s, NASA carried out numerical simulations of Viking [5] and tested their two successful 1975 Viking lander missions to Mars in the Earth's atmosphere in nine separate aircraft drops [6, 7]. In addition to its high cost, the individual atmospheric conditions surrounding each test could not be controlled and would take a long time. The Chinese Academy of Space Technology (CAST) proposed a desired scheme for the heatshield separation. An appropriate ballistic parameter difference was designed to guarantee a positive separation [8, 9]. A Monte Carlo simulation was implemented to analyze the relative distance and relative velocity of the separated part under different conditions. However, unpredictability is inherent in the ejection forces and air resistance during the high-speed separation process. Therefore, further ground tests are necessary to simulate the high-speed separation process and thereby ensure a successful exploration mission.

As we all know, cable-driven mechanisms have several advantages, such as a large workspace with an acceptable cost [10-12], high energy efficiency and heavy load [13-15], simple configuration [16-18], and excellent motion performance [19-21]. This mechanism has a wide range of applications in the field of ground tests. The docking simulator, developed by Langley Research Center, employed a cable-driven mechanism to simulate the docking process in a microgravity environment [22]. The module separation of the Chang'e-5 lunar probe was carried out by a crane with steel cables for ground verification tests [23]. The counterweight balance method was used in the ground test of the lunar sample returner [24]. Therefore, it is a feasible solution to develop and deploy a cable-driven mechanism to simulate the high-speed separation process. However, the above-mentioned docking or separation is so slow that the cable force can be easily controlled. However, during high-speed separation, the highly dynamic characteristics of the system enforce the cable force to undergo violent fluctuations. A study of the force-transmission characteristics of the cable-driven mechanism can facilitate the simulation of the high-speed separation process.

The primary step to reveal the force-transmission characteristics is to model the dynamics with a high initial velocity. Typically, in a large-scale and long-distance cable-driven mechanism, the mass of the cable is notably significant and cannot be ignored [10, 25]. The lumped-mass method is modeled most commonly for mooring system cables [26, 27]. Ref. [28] analyzed backshell separation in a ground test based on a cable-driven mechanism, taking into account the mass of the cable, but short-time separation and high initial velocity have not been discussed. In the short-term separation, the phenomenon of cable slack inevitably occurs, no matter how much the pretension force. Therefore, the phenomenon of cable slack, which plays a significant role in accurately simulating the cable force, should be considered in the dynamic model. In the past decades, considerable attention has been paid to the slack phenomenon of the cable. Vasslos employed the Galerkin method to investigate the nonlinear dynamics of a cable based on the taut-slack problem of small-sagged marine cables [29]. The resultant force of static tension and dynamic tension is less than zero, which means that the cable is in a slack state. Qiao used the LINK180 element in the finite element analysis software ANSYS to simulate the mooring cable [30]. A dynamic model that can reflect the slack characteristics of the cable was established in Refs. [31, 32]. When the cable is in slack condition, the assumption that the cable has a null stiffness is proposed. However, in this paper, the slack of the cable with a high initial velocity is concerned, which differs from the previous work.

Secondly, numerical simulations based on the constructed models were carried out to analyze and improve the performance of the system. Workspace and stability were analyzed by considering dynamic characteristics of cable-driven parallel robots [33]. Parameter analyses with different configurations were discussed on studying the influence of bending stiffness on the cable network's free vibration characteristics [34]. By modifying the optimal parameters of the hanger system, cable fluctuations were suppressed [35]. To study the horizontal vibration characteristics of high-speed elevators, the factors that influenced the horizontal vibration response, such as excitation models, stiffness of guide shoes, and cabin parameters, were analyzed [36]. A trajectory generation method based on input-shaping for under-constrained cable-driven parallel robots was proposed to suppress the unwanted oscillations [37]. The above literature shows the constructive usefulness of considering system parameters and input parameters to explore the characteristics of the system. However, the case of a cable-driven mechanism with high initial velocity has not been considered. In this paper, we focus on the effects of the coefficient matrices and input cable force on the force-transmission characteristics.

The novel contributions of this study are as follows. First, a dynamic model with a slack phenomenon is proposed to illus-

trate the relationship between the input and output cable force. Thereby the force-transmission characteristics of cable are presented. Second, the effects of several parameters, such as thrust, pre-tension, and Young's modulus, on force-transmission characteristics are investigated. Third, an input cable force planning algorithm is proposed to suppress fluctuations in the output cable force.

The rest of the paper is organized as below. Sec. 2 describes the dynamic model of the architecture and force-transmission characteristics. Numerical simulation of the evaluation index and the input cable force planning algorithm is presented in Sec. 3. Two groups of experiments are conducted to verify the correctness of the proposed model in Sec. 4. Conclusions and future work are presented in Sec. 5.

2. Architecture description

2.1 Dynamic modeling of a cable-driven mechanism

A ground simulation test system based on a cable-driven mechanism is shown in Fig. 1. The axial cable is wound on a drum driven by a motor. The centroid of the separated part is located on the extension line of the axial cable. The energy storage spring is located underneath the separated part. The force of the axial cable is $\boldsymbol{F}$ and the thrust of the energy storage spring is $\boldsymbol{F}_{\text{thrust}}$. When the ejection signal is issued, the separated part is accelerated and ejected by the energy storage spring. It can reach a speed of about 5 m/s in a short time (about 30 ms). At the same time, the cable-driven mechanism is activated, accelerating the cable to match the speed of the separated part. The cable is quickly tightened after a short period of slack following the ejection and enters a long-term separation. Due to the high acceleration, the cable force at the drum is not exactly the same as that at the separated part. The study of force-transmission characteristics is conducive to more accurately applying the force to the separated part.

Meanwhile, some assumptions are presented as follows. First, Young's modulus, E, density, ρ, and cross-sectional area, A, of the cable are constant. Second, only the longitudinal vibration along the axial direction of the cable is considered, and the stress components in other directions are zero. The amplitude of the longitudinal vibration of the cable is far less than the length of the cable. Third, the bending moment, damping, friction, and air resistance of the cable are ignored.

The reference configuration, which is the undeformed cable, is an ideal situation, as shown in Fig. 1(a). The actual situation of the cable in the process of movement is shown in Figs. 1(b)-(d). The process from Figs. 1(b) and (c) is a short-term separation with $\boldsymbol{F}_{\text{thrust}}$ and $\boldsymbol{F}$. The process from Figs. 1(c) and (d) is a long-term separation with $\boldsymbol{F}$. The global coordinate system is defined by its origin at point O of the center of the drum cross-section. The y-axis is parallel to the cable, and the direction is downward. The angular location of point P is $\theta(t)$, which is the initial point of contact between the cable and drum. The torque of the motor is τ. The radius of the drum is R. The length of the cable wound around the drum is given by $R\theta(t)$. The length of the cable between the drum and the separated part is given by $l(t)$. The total length of the cable is L_0. Apparently, $L_0 = R\theta(t)+l(t)$. Point Q is the starting point of the axial cable, and point S is the endpoint of the axial cable. The cable element located at $y(t)$ is dy, which varies from 0 to $l(t)$. The elongation of the cable at point $y(t)$ is given by $u(y(t), t)$. When $y(t) = l(t)$, the elongation of the cable at point S is given by $u(l(t), t)$. We assume that the thickness of the cable wound on the drum is negligible compared to R. If J is the moment of inertia of the drum about the x-axis, then the combined moment of inertia of the drum and the cable on it, about the x-axis, is given by $J+\rho R^3\theta(t)$. The cable force at point Q is given by

$$F_{in} = \left[\tau - \rho R^3\dot{\theta}^2 - \left(J + \rho R^3\theta\right)\ddot{\theta}\right]\Big/ R\,. \tag{1}$$

The cable dynamic model has been demonstrated in previous work [28]. We can obtain the second-order ordinary differential equation (ODE).

$$\boldsymbol{M}(t)\ddot{q}(t) + \boldsymbol{C}(t)\dot{q}(t) + \boldsymbol{K}(t)q(t) = \boldsymbol{W}(t) \tag{2}$$

where $q(t)$ is the generalized coordinate relative to $u(y, t)$. The coefficient matrices $\boldsymbol{M}$, $\boldsymbol{C}$, $\boldsymbol{K}$, and $\boldsymbol{W}$ are, respectively, defined as follows.

$$\boldsymbol{U} = \begin{bmatrix} U_{11} & U_{12} & \cdots & U_{1j} & \cdots & U_{1n} \\ U_{21} & U_{22} & & & & \bullet \\ \vdots & & \bullet & & & \bullet \\ U_{i1} & & & \bullet & & \bullet \\ \vdots & & & & \bullet & \\ U_{n1} & \bullet & \bullet & \bullet & & U_{nn} \end{bmatrix} \quad (\boldsymbol{U} = \boldsymbol{M}, \boldsymbol{C}, \boldsymbol{K}) \tag{3}$$

$$M_{ij}(t) = \rho l \int_0^1 \varphi_i \varphi_j d\xi = \frac{1}{2}\rho l(t)\delta_{ij} \tag{4}$$

$$C_{ij}(t) = 2\rho v \int_0^1 (1-\xi)\varphi_i' \varphi_j \mathrm{d}\xi \tag{5}$$

$$K_{ij}(t) = \rho \dot{v} \int_0^1 (1-\xi)\varphi_i' \varphi_j d\xi - \frac{\rho v^2}{l(t)} \int_0^1 (1-\xi)^2 \varphi_i' \varphi_j' d\xi + \frac{EA}{l(t)} \int_0^1 \varphi_i' \varphi_j' d\xi \tag{6}$$

$$W(t) = l(t) \int_0^1 \rho (g - \dot{v}) \varphi_j d\xi \tag{7}$$

$$\varphi(\xi) = \sin(n - 1/2)\pi\xi, n = 1, 2, 3\cdots, \quad \xi = y(t)/l(t)\,. \tag{8}$$

Eq. (8) satisfies the following relation:

$$\int_0^1 \varphi_i(\xi)\varphi_j(\xi)\mathrm{d}\xi = \frac{\delta_{ij}}{2}, \begin{cases} \delta_{ij} = 1, & i = j; \\ \delta_{ij} = 0, & i \neq j. \end{cases} \tag{9}$$

Furthermore, the unique feature of this study is a two-step separation process, which causes different boundary condi-

tions. As for the short-term separation, the boundary conditions are as follows.

$$\begin{cases} t \in [0, 0.03), \\ EAu_y(0,t) = F_{\text{in}}(t), \\ EAu_y(l,t) = mg - m(u_{tt} + \dot{v}) - F_{\text{thrust}}(t). \end{cases} \tag{10}$$

$$u_y = \frac{\delta u}{\delta y}, u_{tt} = \frac{\partial^2 u}{\partial t^2}. \tag{11}$$

As for the long-term separation, the boundary conditions are as follows.

$$\begin{cases} t \in [0.03, 0.3], \\ EAu_y(0,t) = F_{\text{in}}(t), \\ EAu_y(l,t) = mg - m(u_{tt} + \dot{v}). \end{cases} \tag{12}$$

Solving ODE Eq. (2) with numerical methods may yield the $q(t)$. For a given y, the cable force is given by

$$F(y,t) = EAu_y(y,t) = \frac{EA}{l}\boldsymbol{\varphi}'(\xi)\boldsymbol{q}(t). \tag{13}$$

In this work, $y = l$, hence the cable force F_{out} acting on the heatshield can be written as

$$F_{\text{out}} = F(y,t)\big|_{y=l} = EAu_y(l,t) = \frac{EA}{l}\boldsymbol{\varphi}'(1)\boldsymbol{q}(t). \tag{14}$$

In short-term separation, the cable slack phenomenon is handled as follows. When $u(y, t)$ is less than zero, the cable is in a slack state.

$$\begin{cases} F_{out} = EAu_y(l,t) = \dfrac{EA}{l}\displaystyle\sum_{i=1}^{n}\varphi'(1)q(t) & \displaystyle\sum_{i=1}^{n}\varphi'(1)q(t) > 0 \\ F_{out} = EAu_y(l,t) = 0 & \displaystyle\sum_{i=1}^{n}\varphi'(1)q(t) \le 0. \end{cases} \tag{15}$$

2.2 Force-transmission characteristics

High-speed separation is a two-step process: short-term separation and long-term separation. At the end of the short-term separation, the separated part has a high initial velocity, making it a challenge to accurately apply the cable force to the separated part. A dynamic model is established to reveal the relationship between the input and output of cable force. To investigate in-depth this relationship, three key parameters describing the force-transmission characteristics are proposed. The comparison of the output cable and input cable force is shown in Fig. 2, where the output cable force is F_{out}, and the input cable force is F_{in}. Note that the force at the end of the cable is F_{out} and the force at the drum is F_{in}. Therefore, the force-transmission characteristics are as follows.

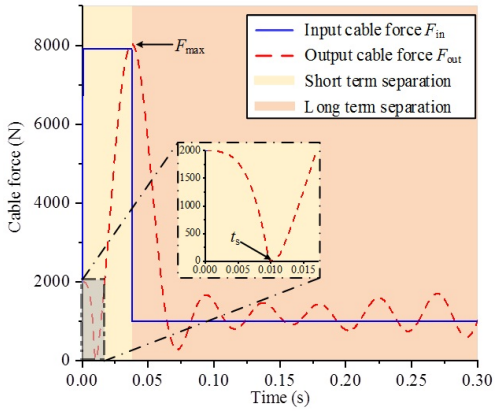

Fig. 2. Comparison of the output cable and input cable force.

First, in the short-term separation stage, the cable inevitably appears slack due to the huge energy generated by the thrust of the energy storage device. If the value of strain is equal to or less than zero, the time, t_s, is defined as the cable slack time. A symbolic parameter of the force-transmission characteristic in this stage is t_s, which is defined as

$$\exists\ t_s \in [0, T] \qquad s.t.\ \ F_{\text{out}}(t_s) = 0. \tag{16}$$

Second, after the cable is slack, the cable force increases until there is a peak cable force, F_{max}, for the separated part with a high velocity. It can be defined as

$$\exists\ t \in [0, T] \qquad s.t.\ \ F_{\text{max}}(t) = \max(F_{\text{out}}). \tag{17}$$

In the short-term separation stage, the kinetic energy and potential energy of the separated part are mainly provided by the energy storage device. The motor mainly does work on the cable and drum.

Third, after the short-term separation is over, the energy storage device no longer does work, and the separated part has a high velocity. The cable-driven mechanism continues to work on the separated part until the end of the long-term separation. The average relative error is ε, which can be given by

$$\varepsilon = \frac{1}{N}\sum_{t=t_1}^{t=t_2}\frac{|F_{\text{out}}(t) - F_{\text{in}}(t)|}{F_{\text{in}}(t)} \times 100\%, \tag{18}$$

where the time when the short-term separation ends is t_1, the time when the long-term separation ends is t_2, the total number of data points in the long-term separation is N. This is an important parameter to evaluate the stability of cable force transmission in the long-term separation stage.

3. Numerical simulation and discussion

According to the proposed dynamic model, the output cable force fluctuation is closely related to the coefficient matrices

and input cable force. The coefficient matrices are determined by the cable-driven mechanism parameters. The significant characteristic of input cable force is a sudden change from short-term separation to long-term separation, resulting in the inaccuracy of output cable force. Thus, the effects of cable-driven mechanism parameters and input cable force planning algorithm are analyzed in this section.

3.1 Effects of the mechanism parameters

To reveal the force-transmission characteristics, parameters, such as the average thrust of the energy storage device, pre-tension, and Young's modulus are explored, respectively.

A comparison of the simulation results of the output cable force with different thrusts is shown in Fig. 3. A partial zoom is illustrated in the subfigure for a detailed output cable force in the short-term separation. The force-transmission characteristics with different thrusts of the energy storage device are summarized in Fig. 4. The results show that the slack time, t_s, decreases with the increase of thrust, because a larger thrust reduces the cable force to zero faster from the same pre-tension. Since the average thrust of the energy storage device determines the acceleration and velocity of the separated part in the short-term separation, the peak cable force is also greatly affected. Both F_{max} and ε increase with the thrust.

The comparison of the simulation results of the output cable force with different pre-tensions is shown in Fig. 5. The force-transmission characteristics with different pre-tensions are summarized in Fig. 6. The simulation results show that the cable slackens more slowly as the pre-tension increases, implying a larger slack time. Another noteworthy point is that the peak cable force is unchanged, which indicates that the pre-tension does not affect the peak cable force. In long-term separation, the increase of the average relative error is relatively small. The above simulation results show that the overall effect of pre-tension on the force-transmission characteristics is not significant. Hence, pre-tension is not a primary consideration in the parameter design.

The comparison of the simulation results of the output cable force with different Young's modulus is shown in Fig. 7. The force-transmission characteristics with different Young's modulus are summarized in Fig. 8. In fact, Young's modulus portrays the stiffness of the cable, implying a faster response for the same deformation, which is also evidenced by the simulation

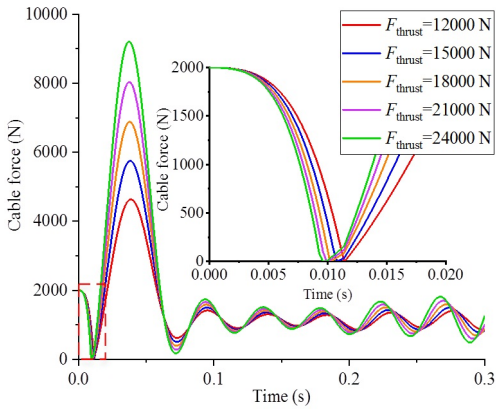

Fig. 3. Comparison of the output cable force with different thrusts.

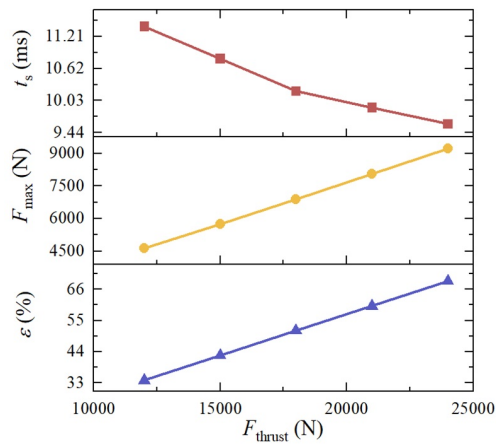

Fig. 4. Force-transmission characteristics with different thrusts (F_{pre} = 2000 N, E = 1.6*10^{11} Pa).

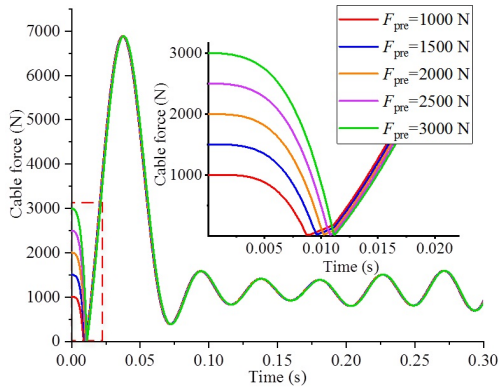

Fig. 5. Comparison of the output cable force with different pre-tension.

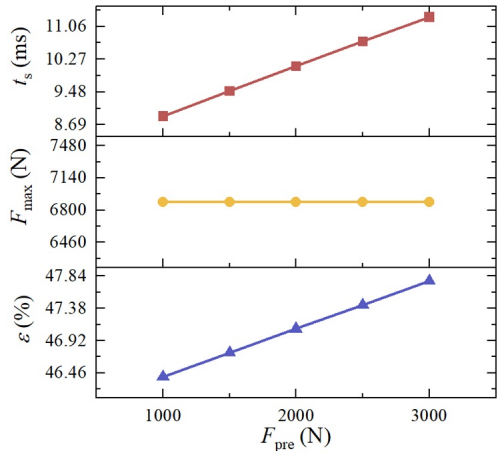

Fig. 6. Force-transmission characteristics with different pre-tensions (F_{thrust} = 21000 N, E = 1.6*10^{11} Pa).

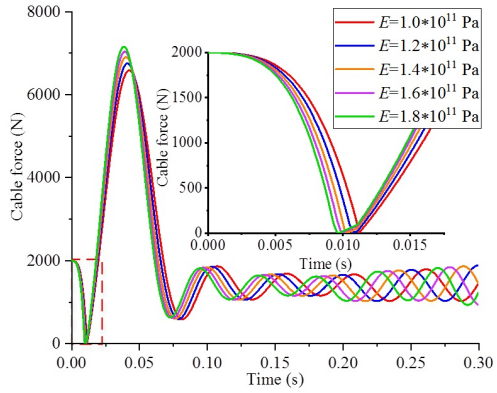

Fig. 7. Comparison of the output cable force with different Young's modulus.

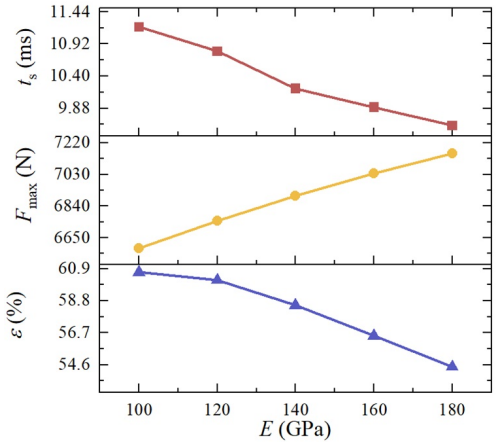

Fig. 8. Force-transmission characteristics with different Young's modulus (F_{thrust} = 21000 N, F_{pre} = 2000 N).

results. Likewise, a larger Young's modulus implies a larger peak cable force. Meanwhile, the average relative error decreases gradually.

A comprehensive consideration of the average thrust of the energy storage device, pre-tension, and Young's modulus on the force-transmission characteristics will provide important guidance for further implementation of the high-speed separation in ground tests.

3.2 Input cable force planning algorithm

In contrast to the above parameters, the input of the cable force has a direct influence on the output of the cable force. As shown in Fig. 2, the cable force decreases suddenly from its peak to a tiny value during the transition from short-term separation to long-term separation, causing a strong jitter in the cable force and poor stability of the cable force applied in the succeeding long-term separation. As a result, this paper proposes an input force planning algorithm to reduce the output cable force fluctuation during the long-term separation process.

The abrupt jitter of the output force is caused by the input force dropping dramatically from short to long-term separation. As a result, implementing a transition function to seamlessly

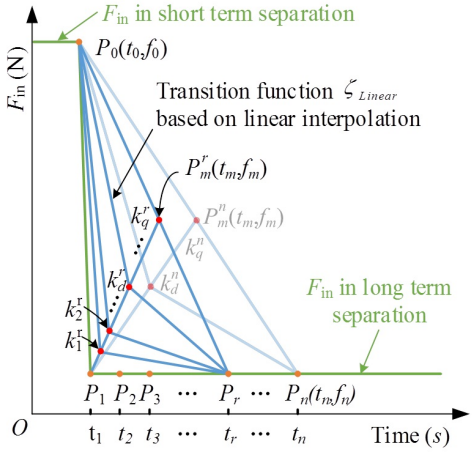

Fig. 9. Introduction of the transition function.

connect the two stages is crucial for reducing jitter. It is worth noting that in the long-term separation stage, the transition function overwrites a portion of the original force without delaying its loading in the timeline. The transition function is schematically shown in Fig. 9. The two ends of the transition function are connected at point P_0 for short-term separation and point P_r for long-term separation, respectively. The short-term separation comes to an end at P_0. The long-term separation begins with P_1. The time corresponding to P_r is defined as the transition time t_r (r = 1, 2, ..., n). The midpoint of P_0 and P_n is P_{mid} (t_{mid}, f_{mid}). The transition point is denoted by k_d^r. Assume that the line segment $P_1P_m^r$ is divided evenly into q segments by the transition points. When the transition time is t_r, the d^{th} transition point is k_d^r. The vector of the transition point is given by

$$\overrightarrow{Ok_d^r} = \overrightarrow{OP_1} + \frac{d \bullet \overrightarrow{P_1P_{mid}^r}}{q}. \tag{19}$$

The transition function can be generated through three reference points, P_0, P_r, and k_d^r. The most common generation method is linear interpolation, which is denoted as $\left\{\zeta_{Linear} : y_{Linear} = \Gamma\left(P_0, P_r, k_d^r\right)\right\}$ in Fig. 9. At the transition point k_d^r, however, the transition function has an inflection point (some degree of sudden shift). When the transition point is the midpoint P_{mid}, i.e., $d = q$, the inflection point does not exist. Thereby, a smoother transition function should be generated by the fitting method to further reduce the fluctuation of the output force. The common fitting methods are linear and nonlinear least squares, whose corresponding typical methods are polynomial fitting ζ_{Poly} and power approximation ζ_{Power}, respectively. Schematic diagrams of ζ_{Poly} and ζ_{Power} with different parameters are shown in Fig. 10.

The typical linear least squares method is a polynomial fit. More reference points $P_L(x_L,y_L)$, where $1 \le L \le km$, on the transition function are produced by interpolation through the

aforementioned three reference points. If we assume that ζ_{Poly} is a polynomial of order *kn*, it can be given by

$$\begin{bmatrix} x_1^{kn} & x_1^{kn-1} & \cdots & 1 \\ x_2^{kn} & x_2^{kn-1} & \cdots & 1 \\ \vdots & \vdots & \ddots & \vdots \\ x_{km}^{kn} & x_{km}^{kn-1} & \cdots & 1 \end{bmatrix} \begin{bmatrix} h_1 \\ h_2 \\ \vdots \\ h_{kn+1} \end{bmatrix} = \begin{bmatrix} y_1 \\ y_2 \\ \vdots \\ y_{km} \end{bmatrix}. \tag{20}$$

Eq. (20) can be rewritten as $\boldsymbol{H} = \boldsymbol{X}^{-1} \bullet \boldsymbol{Y}$, where $\boldsymbol{H}$ is the coefficient matrix of the polynomial and $\boldsymbol{X}$ is called the Vandermonde matrix. Therefore, the transition function for the polynomial fit is as follows.

$$\left\{ \begin{aligned} &\zeta_{Poly} : y_{Poly} = \boldsymbol{H} \bullet x_{Poly}, \\ &x_{Poly} = \begin{bmatrix} x_L^{kn} & x_L^{kn-1} & \cdots & 1 \end{bmatrix}^{\mathrm{T}} \end{aligned} \right\}. \tag{21}$$

The typical nonlinear least squares method is a power approximation. The form of the basis function is $y = ax^b + c$. The parameters *a*, *b*, and *c* are obtained using the least squares method by traversing all reference points P_L. Hence, the transition function of the power approximation is as follows.

$$\left\{ \begin{aligned} &\zeta_{Power} : y_{Power} = a x_{Power}^{\ b} + c, \\ &x_{Power} = \begin{bmatrix} x_L^{kn} & x_L^{kn-1} & \cdots & 1 \end{bmatrix}^{\mathrm{T}} \end{aligned} \right\}. \tag{22}$$

The transition functions with different planning algorithms are shown in Fig. 10. Polynomial fit and power approximation are smoother than linear interpolation.

The primary goal of introducing the transition function is to lessen the fluctuation of the cable force caused by a quick change in the input cable force. The output cable force F_{out}^0 without the planning algorithm first approaches F_{in} at time t_a, as indicated in Fig. 11. The total number of data points from t_a to *T* is N_a. The output cable force with the planning algorithm is F_{out}^{ζ}. For a given input force without a planning algorithm, the two parameters P_0 and P_1 are constants. The transition time t_r and the order *d* of the transition point k_d^r have a significant impact on the expression of the transition function. Typically, when simulating a continuous system on a digital computer, converting it to a discrete form of the problem can improve computational efficiency. In this numerical simulation, the number of transition points is set to *q* = 6 for each transition time t_r. As depicted in Fig. 11, for a linear interpolation transition function ζ_{Linear} with *d* = 3, a transition time t_r that is too small has a negligible effect on lowering the fluctuation of the output force. However, the input force is distorted when the transition time t_r is too large, which in turn raises the inaccuracy of the output force. Similarly, as depicted in Fig. 12, for a linear interpolation transition function ζ_{Linear} with *r* = 4, the same negligible effect also occurs when the order *d* of the transition point is too tiny. To effectively reduce the fluctuation of output force, a suitable selection of transition time t_r and order *d* is required. Thereby, an index to assess the degree of error reduction (DER) is proposed that can filter the ideal transition function parameters. Meanwhile, DER can also be used to evaluate the effectiveness of the input force planning algorithm employed or not.

The degree of error reduction (DER) can be given by

$$\mathrm{DER} = \frac{1}{N_a} \sum_{t=t_a}^{t=T} \frac{\left| F_{\text{out}}^{\zeta}(t) - F_{\text{in}}(t) \right| - \left| F_{\text{out}}^{0}(t) - F_{\text{in}}(t) \right|}{\left| F_{\text{out}}^{0}(t) - F_{\text{in}}(t) \right|}. \tag{23}$$

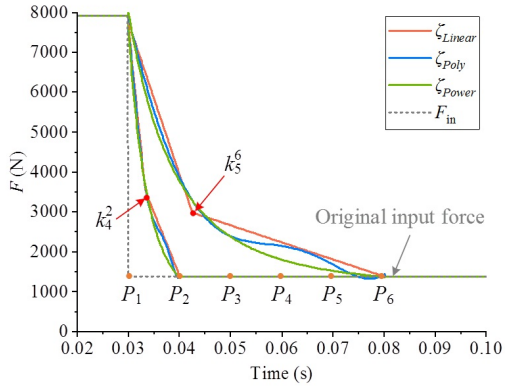

Fig. 10. Transition functions with different planning algorithms.

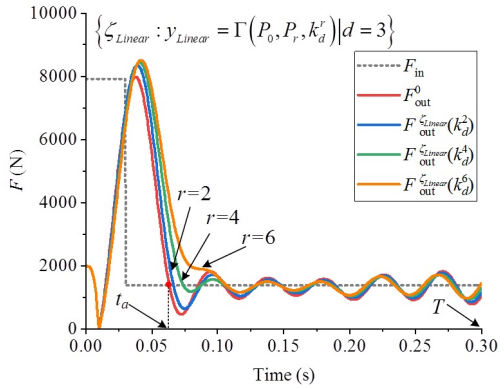

Fig. 11. Effect of transition time on output cable force.

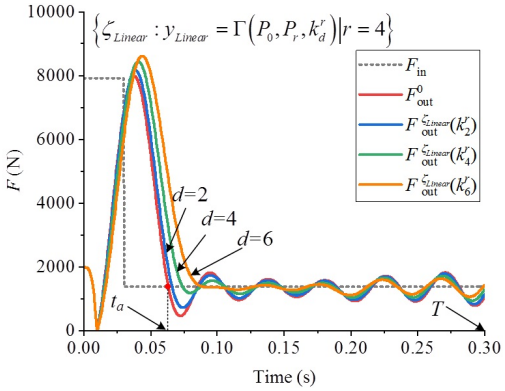

Fig. 12. Effect of transition point on output cable force.

DER is equal to zero if the planning algorithm is not employed $\left(F_{\text{out}}^{\zeta}=F_{\text{out}}^{0}\right)$. The planning algorithm with the t_r and d reduces the fluctuation error of the output force when the DER is less than zero and vice versa. The contours of different planning algorithms concerning DER are shown in Fig. 13. The area enveloped by the contours is called the error optimization capacity (EOC), which can be calculated by the number of parameters that satisfy a specific condition. The EOCs of the three planning algorithms in different conditions are shown in Table 1. Apparently, the blue area (DER < 0) occupies most of the area, indicating that the proposed input force planning algorithm can reduce the fluctuation error of the output force. The EOCs for the three planning algorithms under this condition are 61, 60, and 56, respectively, which is a decreasing trend. It indicates that the planning algorithm ζ_{Linear} with linear interpolation is optimal. The EOCs for the three planning algorithms are 22, 24, and 29, respectively, when DER < -0.2, which is an increasing trend. It indicates that the dark area (DER < -0.2) where the parameters t_r and d are located is a suitable selection that can significantly reduce the fluctuation error of the output force. The simulation results show that the adoption of the input force planning algorithm will significantly reduce the output force fluctuations, which will provide guidance for the future implementation of high-speed separation in ground tests.

4. Prototype implementation

4.1 Experimental setup

A prototype implementation system is shown in Fig. 14. The cable-driven mechanism is used to simulate the high-speed separation process. The energy storage device is composed of a 32-spring array and two annular planes. The spring device is compressed to store energy. One end of the axial cable is driven by a motor. Another end is connected to the separated part via an HBM-U93 force sensor. A guide device is designed to ensure a pure vertical motion. The separated part is equipped with a guide groove, and the spring device is equipped with a guide bar, ensuring that the separation motion has no horizontal component. In addition, we put targets on the separated part, cable, and force sensor to measure displacement and velocity using high-speed cameras. Meanwhile, the encoder of the motor is an additional means of measurement for the cable length. Due to the height limitation of the frame, the separated part cannot be decelerated freely at the end of the experiment and needs to be forced to stop by the deceleration net. The base is fixed on the ground. The properties of the axial cable and the parameters of the experimental system are shown in Table 2.

In face of such a rapidly sharpening input force, dynamic specifications such as acceleration and deceleration of the motor rotating the drum have been considered. The concrete measures are as follows. First, there is no reducer installed between the motor and the drum, but synchronous coupling is used. Second, the drum is made of titanium alloy material with hollow processing, featuring smaller density and higher strength. Third, the time interval Δt from the input signal of the dSPACE controller to the motor response will be considered in the implementation of the experiment.

In a complex and turbulent environment, unpredictability is inherent in the ejection forces and air resistance during the high-speed separation process. By controlling the spring compression, the ejection force can be guaranteed. While the air resistance always varies within a certain range, which contains the upper and lower bounds, in the long-term separation. The upper

Table 1. EOCs of the three planning algorithms in different conditions.

Conditions	ζ_{Linear}	ζ_{Poly}	ζ_{Power}
DER < 0	61	60	56
DER < -0.2	22	24	29

Table 2. Parameters of experimental system.

Parameters	Value	Descriptions
E (Pa)	1.37×10^{11}	Young's modulus
ρ (kg/m)	0.049	Linear density
r_c (mm)	4	Cable radius
R (mm)	55	Drum radius
J (kg·mm^2)	8757	Drum inertia
F_{pre} (N)	2000	Pre-tension

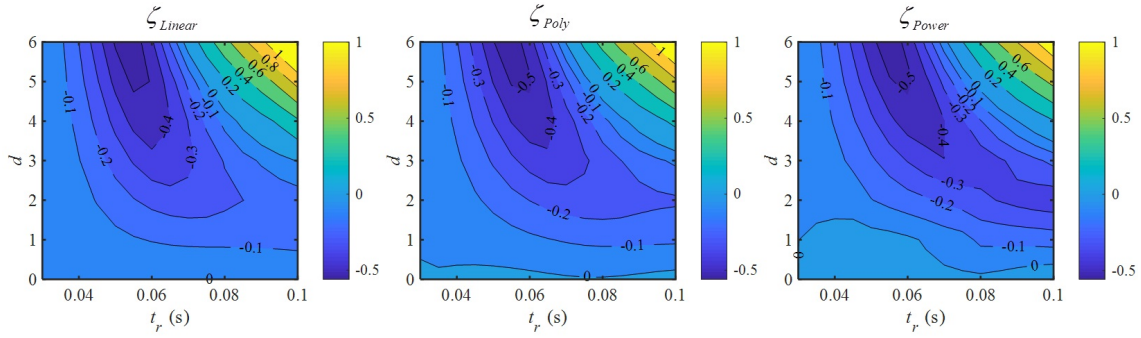

Fig. 13. DERs for linear interpolation (left), polynomial fitting (middle), and power approximation (right).

bound represents the minimum resistance and the maximum separation force, so it is the easiest to separate, and vice versa. For instance, the desired acceleration of the heatshield relative to the lander-parachute is shown in Fig. 15, which was proposed by CAST [8]. They kept the thrusts of the energy storage device consistent in the upper and lower bounds of the short-term separation. In the long-term separation, the acceleration in the upper bound is above zero, obviously, implying a faster separation. While the acceleration in the lower bound is below zero, implying an extreme scenario. To verify the correctness and accuracy of the proposed model, experiments with upper and lower bounds need to be carried out.

4.2 Experimental results

The high-speed separation process is shown in Fig. 16. The separated part starts at the moment when the ejection command is issued, as shown in Fig. 16(a). At the same time, the motor of the cable-driven mechanism starts. The compressed spring device generates a large thrust in the short-term separation. The displacement of short-term separation is Δd. After T = t1, the separated part is pulled upward by the cable-driven mechanism. The displacement of long-term separation is ΔL.

The comparison of the experimental and desired displacements in the upper and lower bounds is shown in Fig. 17. The experimental displacements in the upper and lower bounds are ΔL_{Upper} and ΔL_{Lower}, respectively. The results show that they are in good agreement with the desired displacements. The comparison of the experimental and desired velocities in the upper and lower bounds is shown in Fig. 18. The separated part is accelerated in the short-term separation by the ejection force of the spring device. Concretely, the comparison of displacement and velocity in the upper and lower bounds is listed in Table 3. The velocities at the end of short-term separation and long-term separation are V_s and V_l, respectively. In the short-term separation, the displacement of the separated part is much larger compared to the desired value. The larger displacement

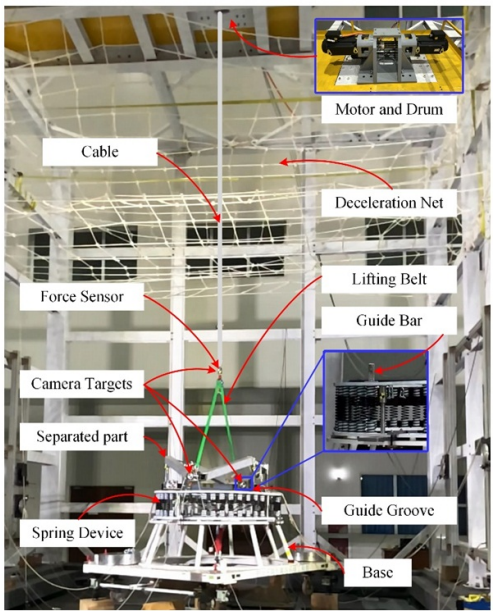

Fig. 14. Prototype implementation system.

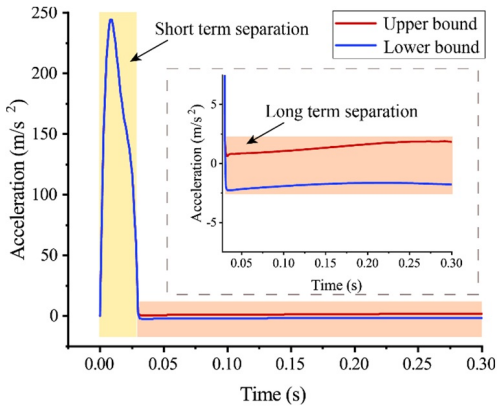

Fig. 15. Desired acceleration of the heatshield relative to the lander-parachute.

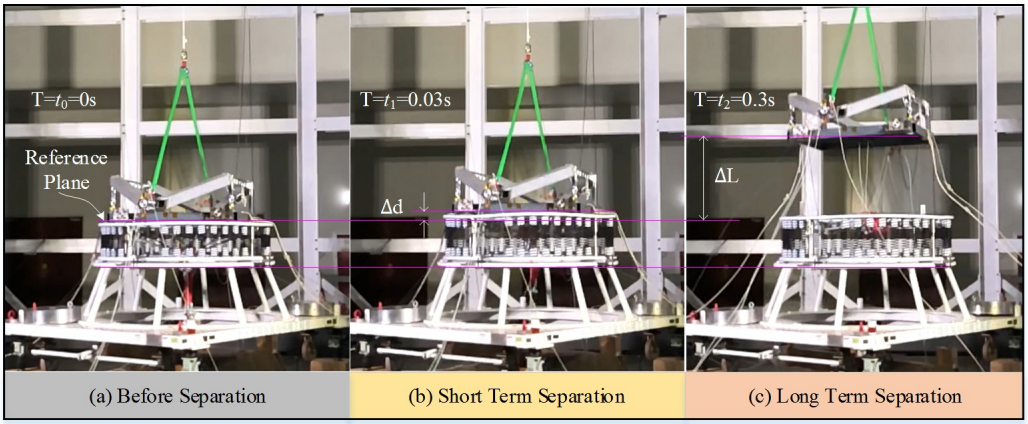

Fig. 16. The high-speed separation process of the separated part.

Table 3. Comparison of displacement and velocity in the upper and lower bounds.

Symbol	Δd (m)		ΔL (m)		V_s (m/s)		V_l(m/s)	
Bound	Upper	Lower	Upper	Lower	Upper	Lower	Upper	Lower
Experimental value	0.118	0.117	1.371	1.220	4.746	4.264	5.152	4.047
Desired value	0.081	0.081	1.426	1.314	4.801	4.801	5.204	4.340
Relative error (%)	45.67	44.44	-3.86	-7.15	-1.15	-11.18	-1.00	-6.75
Absolute error	0.037	0.036	-0.055	-0.094	-0.055	-0.537	-0.052	-0.293

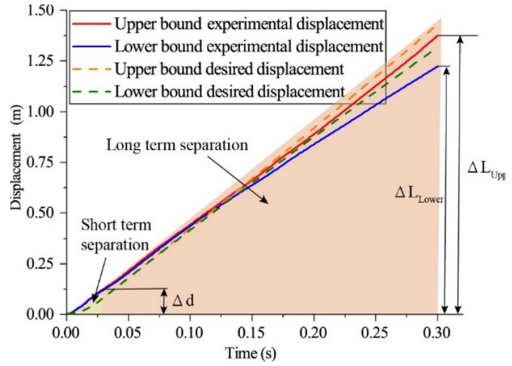

Fig. 17. Displacements in the upper and lower bounds.

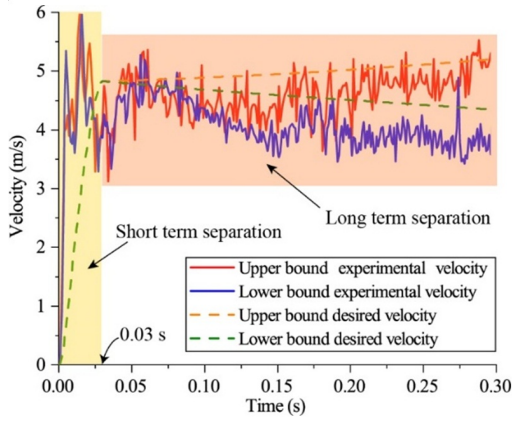

Fig. 18. Velocities in the upper and lower bounds.

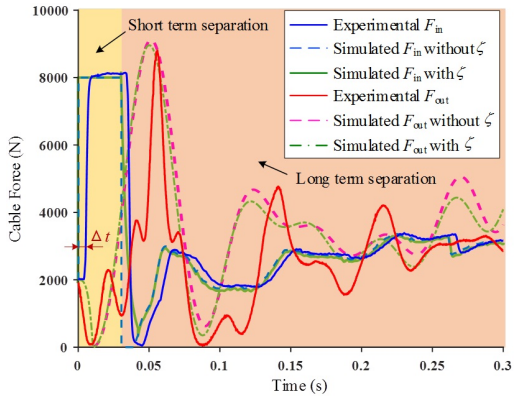

Fig. 19. Comparison of the output and input cable force in the upper bound.

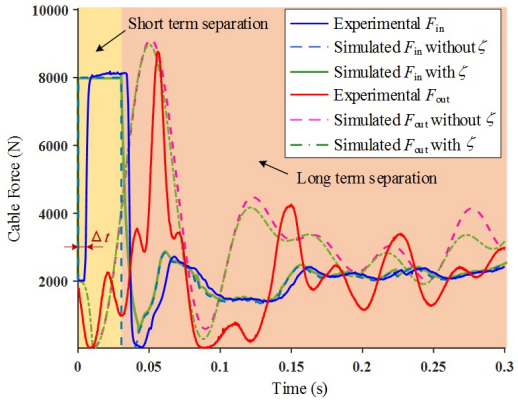

Fig. 20. Comparison of the output and input cable force in the lower bound.

error in short-term separation is caused by a small number of the divider. Thus, the absolute error data is also presented together in Table 3. Furthermore, the relative displacement and relative velocity at the end of the high-speed separation process are of primary interest. In the long-term separation, the displacement and velocity of the separated part are slightly smaller than the desired value, which may be due to the existence of friction. The relative errors of the displacement in the upper and lower bounds at the end of the separation are -3.86 % and -7.15 %, respectively. The relative errors of the velocity in the upper and lower bounds at the end of the separation are -1.00 % and -6.75 %, respectively. The errors of the experimental results are less than 10 %, satisfying the requirements proposed by CAST.

Figs. 19 and 20 show the experimental results for the upper and lower bound. The results show that there is a time delay Δt between the simulated F_{in} and the experimental F_{in}. When the ejection command is triggered, the controller receives the start signal from the motor. The signal passes through the driver and is sent to the motor. Then the torque sensor at the motor receives this signal and returns it to the data acquisition instrument at the controller. The time spent by the above process is a time delay, Δt. The delay is inherent in the system and is only about 0.0045 s. The effect on this separation is negligible.

The blue dashed line is a theoretical input, which cannot be used directly as an input of the system. The reason for this is that the sudden decrease of the cable force causes a sharp fluctuation, which was discussed in Sec. 3. Therefore, we

Table 4. Force-transmission characteristics in the upper and lower bounds.

Force-transmission characteristics		t_s (ms)	F_{max} (N)	ε (%)
Upper bound	Experimental value	9.7	8809.81	33.67
	Desired value	10.4	8959.29	36.93
	Relative error	-6.73 %	-1.66 %	-8.82 %
	Absolute error	-0.7	149.48	-3.26
Lower bound	Experimental value	9.1	8759.76	41.85
	Desired value	10.4	8966.77	43.91
	Relative error	-12.50 %	-2.31 %	-4.69 %
	Absolute error	-1.3	-207.01	-2.06

Table 5. Comparison between this study and the previous study.

Terms	This study	Previous study
Application scenarios	Focus on high-speed separation with initial velocity, including short term separation and long-term separation.	Focus on high-acceleration separation at stationary state.
Cable slack	Short term separation with cable slack	No cable slack
Force-transmission characteristics	Cable slack time, peak cable force, and average relative error	Overshoot, response time, and average relative error
Influence factors	Thrust of the energy storage device, pre-tension, and Young's modulus.	Load, pre-tension, and cable parameters.
Input planning algorithm	Input cable force planning algorithm to reduce fluctuation.	No input planning algorithm

adopted a transition function ζ with parameters t_r and d of 0.04 and 5, respectively. The green solid line indicates the simulated input obtained by the transition function, which is the real input of the system. The green dotted line indicates the simulated output with transition function, obviously, which is better than the simulated output without transition function. The force-transmission characteristics provide a well evaluated relationship between the input and output cable force. Therefore, the slack time, peak cable force, and average relative error are obtained. Furthermore, to evaluate the accuracy of the proposed model, the relative and absolute errors of the force-transmission characteristics are introduced, which are listed in Table 4. Due to a very small divisor, the relative error of the slack time of the lower bound is -12.50 %. In fact, the absolute error is only 1.3 ms, which is perfectly acceptable. Moreover, the maximum errors of F_{max} and ε are -2.31 % and -8.82 %, respectively, indicating the correctness of the proposed model.

However, the output results of the simulations and experiments do not seem to match well compared to the input results. It is worth noting that there is an energy explosion in the short-term separation, making the output following control a very difficult problem. A model of cable dynamics considering slack phenomena is central to the solution of the above problem. However, the perfect following of the output cable force is also affected by various factors such as model simplification, air resistance, friction, and the vibration of the lifting belts. Considering the above factors to construct a more accurate model will be our future work.

5. Conclusion

A cable-driven mechanism is proposed to simulate the heat-shield separation in ground tests. Facing the difficulty of a high initial velocity at the end of the short-term separation, force-transmission characteristics were studied to reveal the relationship between the input and output cable force. Three characteristic parameters, such as slack time, peak cable force, and average relative error, were proposed. In addition, the effects of thrust, pre-tension, and Young's modulus on force-transmission characteristics were investigated. Also, an input force planning algorithm was proposed to further reduce the fluctuation of the output cable force. The numerical simulation analysis including mechanism parameters and input cable forces provided guidance and solutions for improving the performance of force-transmission characteristics.

A series of ground tests for high-speed separation was implemented. The results show that the errors of both displacement and velocity at the end of separation are less than 10 %, which verifies the feasibility of this experimental scheme. The relative and absolute errors of the force-transmission characteristics were introduced in the upper and lower bounds to prove the correctness of the proposed model in this paper. In summary, the main work of this paper is listed in Table 5, which also clearly emphasizes the advancement compared to the previous study.

However, the incomplete match between the experimental and simulated output is due to model simplification, friction, and the vibration of lifting belts, which will be considered to construct a more accurate model in future studies. Completely

simulating the high-speed separation process will ensure a novel theoretical basis, which can be used in the future to help maintain the safety of the lander.

Acknowledgments

This work was supported by the National Natural Science Foundation of China (Grant No. 51975044 and No. 51975307) and the China Postdoctoral Science Foundation (Grant No. 2022M711804).

Nomenclature

A : Cross-sectional area of cable
d : Sample number of the transition point
DER : Degree of error reduction
dy : Cable element at y
EOC : Error optimization capacity
E : Young's modulus
$\boldsymbol{F}$: Cable force
F_{pre} : Pre-tension
F_{thrust} : Thrust of the energy storage device
F_{in} : Cable force at point Q
F_{out} : Cable force at point S
$\boldsymbol{H}$ and $\boldsymbol{X}$: Vandermonde matrix and coefficient matrix of the polynomial
J : Drum inertia about the x-axis
k_d^r : Transition point
l : Length of the cable between the drum and the separated part
L_0 : Total length of the cable
m : Mass of the separated part
$\boldsymbol{M}$, $\boldsymbol{C}$, $\boldsymbol{K}$, and $\boldsymbol{W}$: Mass, damping, stiffness, and external force matrices, respectively
N : Total number of data points in the long-term separation
P_r : Sample point of the original input
P_L : Reference points
q : Generalized coordinate relative to u
r : Sample number of the transition time
R : Radius of the drum
r_c : Radius of the cable
t : Time
t_1 and t_2 : Time when the short-term and long-term separation ends
t_r : Transition time
t_s : Cable slack time
T : End time
u and u ($y(t)$, t): Elongation of the cable
u_t and u_y : Derivative of u with respect to t and y
u_{tt} : Second order derivative of u with respect to t
v : Speed of the cable
ρ : Density of the cable
θ : Angular location of point P
τ : Torque of the motor
ε : Average relative error
Δd : Displacement of short-term separation
ΔL : Displacement of long-term separation
Δt : Time delay
ζ_{Linear} : Transition function of the linear interpolation
ζ_{Poly} : Transition function of the polynomial fitting
ζ_{Power} : Transition function of the power approximation

References

[1] S. Hou, H. Sun, Q. Li and X. Tang, Design and experimental validation of a disturbing force application unit for simulating spacecraft separation, *Aerospace Science and Technology*, 113 (2021) 106674.
[2] J. Lingard and M. Darley, Simulation of parachute fluid structure interaction in supersonic flow, *18th AIAA Aerodynamic Decelerator Systems Technology Conference and Seminar* (2005).
[3] I. Rountree, D. Yaghoubi and S. Maynor, Integrated design for the MSR SRC mars ascent vehicle, *2022 IEEE Aerospace Conference*, Munich, Germany (2022).
[4] B. Raiszadeh, P. Desai and R. Michelltree, Mars exploration rover heat shield recontact analysis, *21st AIAA Aerodyn, Decelerator Syst. Technol. Conf.* (2011) 2584.
[5] H. P. Klein, Simulation of the Viking biology experiments: an overview, *J. of Molecular Evolution*, 14 (1979) 161-165.
[6] H. Murrow, C. Eckstrom and D. Henke, Development flight tests of the Viking decelerator system, *4th Aerodynamic Deceleration Systems Conference*, Palm Springs, USA (1973) 455.
[7] R. Moog, R. Bendura, J. Tlmmons and R. Lau, Qualification flight tests of the Viking decelerator system, *J. of Spacecraft and Rockets*, 11 (1974) 188-195.
[8] C. Zheng, Research on mars EDL dynamic modeling, guidance and control method, *Master's Thesis,* Harbin Institute of Technology (2020).
[9] D. Chen, Simulation and analysis of mars entry parachute descent phase dynamics, *Master's Thesis,* Haibin Institute of Technology (2016).
[10] X. Tang and R. Yao, Dimensional design on the six-cable driven parallel manipulator of FAST, *J. of Mechanical Design*, 133 (11) (2011) 111012.
[11] A. Walsh and J. R. Forbes, Modeling and control of a wind energy harvesting kite with flexible cables, *2015 American Control Conference (ACC)* (2015) 2383-2388.
[12] H. Sun, S. Hou, Q. Li and X. Tang, Research on the configuration of cable-driven parallel robots for vibration suppression of spatial flexible structures, *Aerospace Science and Technology*, 109 (2021) 106434.
[13] W. Zhu and H. Ren, An accurate spatial discretization and substructure method with application to moving elevator cable-car systems — part I: methodology, *J. of Vibration Acoustics*, 135 (5) (2013) 051036.
[14] Q. Zhang, Y. Yang, T. Hou and R. Zhang, Dynamic analysis of high-speed traction elevator and traction car-rope time-varying system, *Noise Vibration Worldwide*, 50 (2019) 37-45.
[15] J. Xu, M. Miao and S. Zheng, Modeling and analysis of rope flexibility in deep sea lifting operations, *2018 IEEE International Conference on Mechatronics and Automation (ICMA)*, Chang-

chun, China (2018) 767-772.
[16] L. Barbazza, D. Zanotto, G. Rosati and S. K. Agrawal, Design and optimal control of an underactuated cable-driven micro-macro robot, *IEEE Robotics Automation Letters*, 2 (2017) 896-903.
[17] X. Zheng, X. Zhu, Z. Chen, X. Wang, B. Liang and Q. Liao, An efficient dynamic modeling and simulation method of a cable-constrained synchronous rotating mechanism for continuum space manipulator, *Aerospace Science and Technology*, 119 (2021) 107156.
[18] D. Gueners, H. Chanal and B.-C. Bouzgarrou, Design and implementation of a cable-driven parallel robot for additive manufacturing applications, *Mechatronics*, 86 (2022) 102874.
[19] P. Lambert, L. Da Cruz and C. Bergeles, Design, modeling, and implementation of a 7-DOF cable-driven haptic device with a configurable cable platform, *IEEE Robotics Automation Letters*, 5 (2020) 5764-5771.
[20] X. Li, J. Zhang and J. Han, Trajectory planning of load transportation with multi-quadrotors based on reinforcement learning algorithm, *Aerospace Science and Technology*, 116 (2021) 106887.
[21] Y. Liu, F. Zhang, P. Huang and X. Zhang, Analysis, planning and control for cooperative transportation of tethered multi-rotor UAVs, *Aerospace Science and Technology*, 113 (2021) 106673.
[22] J. E. Pennington, *Langley Research Center Simulators and Studies Related to Space Rendezvous and Docking*, NASA, USA (1964).
[23] D. Ren, Q. Li, Z. Zhang, Y. Du, H. Huang and Y. Shu, Ground-test validation technologies for Chang'e-5 lunar probe, *Scientia Sinica Technologica*, 51 (2021) 778-787.
[24] H. Li, G. Wang, S. Xu, W. Lei and L. Zhang, Analysis and terrestrial verification of separation resistance of lunar sampling and re-entry capsule, *Spacecraft Environment Engineering*, 34 (2017) 662-666.
[25] A. Rouvinen, T. Lehtinen and P. Korkealaakso, Container gantry crane simulator for operator training, *Proceedings of the Institution of Mechanical Engineers, Part K: J. of Multi-body Dynamics*, 219 (2005) 325-336.
[26] R. J. Caverly and J. R. Forbes, Dynamic modeling and non-collocated control of a flexible planar cable-driven manipulator, *IEEE Transactions on Robotics*, 30 (2014) 1386-1397.
[27] R. J. Caverly, J. R. Forbes and D. Mohammadshahi, Dynamic modeling and passivity-based control of a single degree of freedom cable-actuated system, *IEEE Transactions on Control Systems Technology*, 23 (2014) 898-909.
[28] S. Hou, X. Tang, H. Sun, Y. Wang and Q. Li, Analysis of cable-force transmission characteristics and disturbing force/ moment of high-acceleration cable-driven parallel mechanism, *IEEE/ ASME Transactions on Mechatronics*, 27 (1) (2022) 348-359.
[29] D. Vassalos and S. Huang, Dynamics of small-sagged taut-slack marine cables, *Computers Structures*, 58 (1996) 557-562.
[30] D. Qiao, J. Yan, H. Liang, D. Ning, B. Li and J. Ou, Analysis on snap load characteristics of mooring line in slack-taut process, *Ocean Engineering*, 196 (2020) 106807.
[31] M. A. Jordán and J. L. Bustamante, Numerical stability analysis and control of umbilical-ROV systems in one-degree-of-freedom taut-slack condition, *Nonlinear Dynamics*, 49 (2007) 163-191.
[32] Y. Tang, R. Zhang, N. Cheng and J. Zhao, Analysis of snap tension of deep water mooring with lumped mass method, *J. of Tianjin University*, 42 (2009) 695-701.
[33] J. Heo, B. Park, J. Park, C. Kim, J. Jung and K. Park, Workspace and stability analysis of a 6-DOF cable-driven parallel robot using frequency-based variable constraints, *J. of Mechanical Science and Technology*, 32 (2018) 1345-1356.
[34] W. Chen, Z. Zhang, X. Zhen and M. Li, Effect of bending stiffness on the in-plane free vibration characteristics of a cable network, *J. of Mechanical Science and Technology*, 34 (2020) 4439-4463.
[35] S. Farahmand-Tabar and M. Barghian, Formulating the optimum parameters of modified hanger system in the cable-arch bridge to restrain force fluctuation and overstressing problems, *J. of the Brazilian Society of Mechanical Sciences and Engineering*, 42 (2020) 453.
[36] D. Song, P. Zhang, Y. Wang, C. Du, X. Lu and K. Liu, Horizontal dynamic modeling and vibration characteristic analysis for nonlinear coupling systems of high-speed elevators and guide rails, *J. of Mechanical Science and Technology*, 37 (2023) 643-653.
[37] S. W. Hwang, J. Bak, J. Yoon, J. H. Park and J. Park, Trajectory generation to suppress oscillations in under-constrained cable-driven parallel robots, *J. of Mechanical Science and Technology*, 30 (2016) 5689-5697.

Senhao Hou received the Ph.D. in Mechanical Engineering from Tsinghua University, Beijing, China, in 2021. He is a postdoctoral of the Department of mechanical engineering, Tsinghua University, Beijing, China. His research interests include cable robots and force control.

Dongxing Li received the B.S. from Tsinghua University, Beijing, China, in 2019. He is currently a Ph.D. candidate in Mechanical Engineering, Tsinghua University, Beijing, China. His research interests are cable robots and robot control.

Qunzhi Li received the Ph.D. in Mechanical Engineering from Tianjin University, Tianjin, China, in 2007. She is currently a senior engineer of Beijing Institute of Spacecraft System Engineering. Her research interests are spacecraft overall design, space robot, and other related work.

Xiaoqiang Tang received the Ph.D. in Mechanical Engineering from Tsinghua University, Beijing, China, in 2001. He is currently a Professor of Mechanical Engineering, Tsinghua University. His research interests include parallel manipulators, robots, and reconfigurable manufacturing technology.